Three-dimensionality in the wake of a rotating cylinder in a uniform flow

A. Rao[1], J. Leontini[1,†], M. C. Thompson[1] and K. Hourigan[1,2]

[1]Fluids Laboratory for Aeronautical and Industrial Research (FLAIR), Department of Mechanical and Aerospace Engineering, Monash University, Melbourne, Victoria 3800, Australia

[2]Division of Biological Engineering, Monash University, Melbourne, Victoria 3800, Australia

The wake of a rotating circular cylinder in a free stream is investigated for Reynolds numbers $Re \leqslant 400$ and non-dimensional rotation rates of $\alpha \leqslant 2.5$. Two aspects are considered. The first is the transition from a steady flow to unsteady flow characterized by periodic vortex shedding. The two-dimensional computations show that the onset of unsteady flow is delayed to higher Reynolds numbers as the rotation rate is increased, and vortex shedding is suppressed for $\alpha \geqslant 2.1$ for all Reynolds numbers in the parameter space investigated. The second aspect investigated is the transition from two-dimensional to three-dimensional flow using linear stability analysis. It is shown that at low rotation rates of $\alpha \leqslant 1$, the three-dimensional transition scenario is similar to that of the non-rotating cylinder. However, at higher rotation rates, the three-dimensional scenario becomes increasingly complex, with three new modes identified that bifurcate from the unsteady flow, and two modes that bifurcate from the steady flow. Curves of marginal stability for all of the modes are presented in a parameter space map, the defining characteristics for each mode presented, and the physical mechanisms of instability are discussed.

Key words: parametric instability, vortex shedding, wakes/jets

---

1. Introduction

The flow past a rotating cylinder is a function of two non-dimensional parameters. These are the Reynolds number, $Re = UD/\nu$, where U is the free-stream velocity, D is the cylinder diameter, and ν is the kinematic viscosity, and the non-dimensional rotation rate $\alpha = \omega D/2U$, where ω is the rotational speed of the cylinder. This latter parameter is therefore the ratio of the surface velocity of the cylinder to the free-stream velocity.

Flow past a non-rotating circular cylinder in the low-Reynolds-number range and the bifurcations from one state to another have been extensively studied, and several regimes of flow have been identified. Experimental work on the transition between the steady and unsteady regimes has been discussed by Williamson (1996*b*) and others. Numerical investigations have also contributed to the understanding of the flow. Several research groups, e.g. Barkley & Henderson (1996), Karniadakis &

† Email address for correspondence: justin.leontini@monash.edu

Triantafyllou (1992) and Thompson, Hourigan & Sheridan (1996), have investigated the transition from two-dimensional vortex shedding to three-dimensional flow at $Re \simeq 190$, where the wake vortices develop a waviness in the spanwise direction at a wavelength of around $4D$. This wake instability is known as mode A (Williamson 1988), which has also been shown to be the saturated form of a linear mode growing on the two-dimensional periodic base flow (Barkley & Henderson 1996). Further increasing Re sees a second type of three-dimensional flow develop, with fine-scale (a wavelength of around $0.8D$ in the spanwise direction) streamwise vortices developing in the braid shear layers between wake vortices. This instability is known as mode B (Williamson 1988). Even though in reality this flow develops from the already three-dimensional mode A wake, it is also well described by a linear mode growing on the two-dimensional base flow (Barkley & Henderson 1996). The linear modes corresponding to modes A and B are commensurate with the base flow, introducing no new frequencies. However, modes which are incommensurate with the base flow has also been observed in the wakes of cylinders. Owing to the introduction of a second frequency, this mode is expected to be quasi-periodic, and so is designated mode QP (Blackburn, Marques & Lopez 2005). Such modes have also been observed in wakes of square cylinders (Blackburn & Lopez 2003) and transversely oscillating cylinders (Leontini, Thompson & Hourigan 2007).

The effect of rotation is to cause opposing viscous effects on either side of the cylinder centreline. Depending on the rotation rate, the flow may remain attached on one side of the cylinder while separating from the other, causing a net lift force directed away from the side where the flow remains attached. This is known as the Magnus effect (Prandtl 1926). Some of the earliest numerical investigations (Ingham 1983; Badr, Dennis & Young 1989) were primarily used for comparison with experimental work, and were performed for $Re \leqslant 100$. The classifications were primarily aimed at differentiating the steady and unsteady regimes of flow by varying the rotation rate and Reynolds numbers. Vortex shedding was found to be suppressed for $\alpha \geqslant 2$ at $Re = 1000$ (Badr *et al.* 1990; Chew, Cheng & Luo 1995), while a single-sided vortex shedding regime was observed by Chen, Ou & Pearlstein (1993) over a short time history. Similar findings were also observed for $\alpha \leqslant 2.5$ and $Re \leqslant 200$ by Kang, Choi & Lee (1999), who distinguished regions of flow stability. They further quantified the lift and drag coefficients over this regime.

When the parameter range was further increased to higher rotation rates of $\alpha < 12$, a secondary shedding regime was observed by Stojković, Breuer & Durst (2002). On increasing the rotation rate at $Re = 100$, the Kármán-type shedding ceased at $\alpha = 1.8$ until higher rotation rates when shedding reappeared over a narrow range of $4.8 \leqslant \alpha \leqslant 5.15$. The boundaries of this secondary shedding regime were later identified in a subsequent investigation (Stojković *et al.* 2003). This shedding was first observed around $\alpha \simeq 4.3$ (Mittal & Kumar 2003) at $Re = 200$; the Reynolds number range of occurrence decreased as the rotation rate was increased to higher values. Recent numerical simulations by Akoury *et al.* (2008) showed that the secondary shedding regime occurred over a broader range at higher Reynolds number. The vortex shedding in this regime was single sided and the shedding frequency was observed to be much lower compared with the two-sided Kármán shedding at lower rotation rates. Beyond $\alpha \simeq 5.5$, steady flow was observed (Pralits, Brandt & Giannetti 2010). Recent experimental visualizations by Kumar, Cantu & Gonzalez (2011) confirmed the two shedding regimes and the shedding frequencies observed in the two shedding regimes were in good agreement with previous numerical work. However, little is known about the three-dimensional structure of the wake at these rotation rates.

The cylinder rotation not only alters the two-dimensional flow structure, the three-dimensional modes present in the wake are also altered. The onset of three-dimensionality for rotation rates of $\alpha > 0$ had not been investigated until recently, although it has been generally stated that the flow is three-dimensional for $Re \gtrsim 200$. Direct numerical simulations were performed by Akoury *et al.* (2008) for $\alpha \leqslant 1.5$ and $Re \leqslant 300$. When the rotation rate was increased to $\alpha = 0.5$, the onset of three-dimensionality occurred at $Re \simeq 220$, with the appearance of mode A type structures in the wake. This mode was found to persist up to $Re = 300$, with a spanwise wavelength of approximately $4D$. The onset of three-dimensional flow is delayed to higher Reynolds numbers on increasing the rotation rate. At $\alpha = 1.5$ and $Re = 200$, the flow was found to be two-dimensional.

The effect of three-dimensional instabilities at higher rotation rates has been investigated by Mittal (2004) for $\alpha = 5$ at $Re = 200$. The two-dimensional flow field is steady while the three-dimensional simulations show the growth of centrifugal instabilities along the span of the cylinder. They also tested the effect of various boundary conditions for cylinders of different aspect ratios (the ratio of the cylinder diameter to its length). For aspect ratios of 5, 10 and 15 with slip walls, the time history of the drag coefficient showed oscillatory behaviour. The flow around the cylinder with lower aspect ratio and slip walls resembled two-dimensional flow (which was steady). However, larger-aspect-ratio cylinders with no-slip walls showed fluctuations, primarily because of the interaction of the boundary layer of the wall and the rotating cylinder. The three-dimensional flow was associated with centrifugal instabilities of around $1D$ spanwise wavelength. This instability was predicted to cause a reduction in lift and increase in drag coefficient.

When the spatio-temporal symmetry of the vortex street is broken (as occurs when the cylinder is rotating), further modes become possible. In particular, subharmonic modes which repeat over two cycles of the two-dimensional base flow can occur. Such a mode is termed subharmonic and has been detected in the wake of a circular cylinder with a control wire (Zhang *et al.* 1995), in the wake of an inclined square cylinder (Sheard, Fitzgerald & Ryan 2009; Sheard 2011), in oscillating cylinder wakes Leontini *et al.* (2007), and in the wakes of rings (Sheard, Thompson & Hourigan 2003, 2005*a*; Sheard *et al.* 2005*b*). It is expected that similar modes should occur for rotating cylinders.

Recent linear stability investigations were undertaken by Meena *et al.* (2011), at $Re = 200$ for $3 \leqslant \alpha \leqslant 5$. They observed three-dimensional modes with a purely real growth rate for $\alpha \leqslant 4.3$, while a complex three-dimensional mode was observed for $\alpha > 4.5$. Their three-dimensional investigations showed what appear to be centrifugal instabilities near the cylinder and the time histories of the force coefficients indicated that this flow is aperiodic.

All of these previous studies indicate that the flow is a function of both Re and α, with a wide variety of vortex shedding regimes and three-dimensional modes occurring. The current study therefore considers systematically the wakes of rotating cylinders as a function of both these variables. The remainder of this article is organized as follows. After a brief problem definition in § 2 the numerical method employed in our investigations is detailed in § 3, supplemented by validation studies. This is followed by the presentation of results. In that section, first the two-dimensional flow structures observed as a function of Re and α are described in § 4. Particular attention is paid to the transition from steady to unsteady flow. This is followed by the results of a linear stability analysis in § 5, investigating the transition to three-dimensional flow from the established two-dimensional flows. Curves of marginal stability of each of
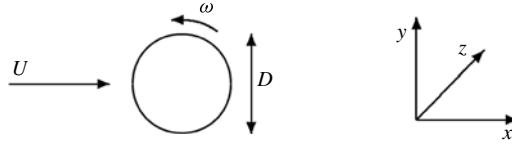
FIGURE 1. Schematic representation of the spinning cylinder in a free stream.

these three-dimensional modes are presented in the *Re–α* plane, and the characteristics of each of these modes are described. Physical mechanisms of instability are proposed for a number of these modes. This is followed by some concluding remarks.

2. Problem definition

A schematic diagram of the problem under consideration is shown in figure 1. The cylinder of diameter D spins in an anticlockwise sense at a constant angular velocity, ω. The oncoming uniform flow velocity is represented by U. Results for $0 \leqslant Re \leqslant 400$ and $0 \leqslant \alpha \leqslant 2.5$ are presented.

3. Numerical formulation

3.1. *Fluid flow equations*

For the base flow, the incompressible Navier–Stokes equations are solved in two dimensions using a spectral-element approach. The computational domain consists of quadrilateral elements which are concentrated in the regions of high velocity gradients to accurately capture the flow dynamics. The boundaries of these quadrilateral elements are straight except in the vicinity of the cylinder, where curved edges are used to accurately represent the circular cylinder. These elements are further subdivided with internal node points distributed according to the Gauss–Legendre–Lobatto quadrature points, with the velocity and pressure fields represented by tensor products of Lagrangian polynomial interpolants. Despite being only formally C_0-continuous across element boundaries, these methods are known to provide spectral convergence as the polynomial order is increased (Karniadakis & Sherwin 2005). The number of node points within each element ($N \times N$) can be specified at runtime with the interpolating polynomial order in each direction being $N - 1$. A second-order fractional time-stepping technique is used to sequentially integrate the advection, pressure and diffusion terms of the Navier–Stokes equations forward in time. The unsteady solver is used to investigate the parameter range covering both the steady and unsteady regimes of flow.

More details of the solver can be found in Thompson *et al.* (2006*a*); and the solver has been previously used in studies of bluff-body flows (Thompson *et al.* 1996, 2006*b*; Leontini *et al.* 2007) and of flows over rolling cylinders near a wall (Stewart *et al.* 2006, 2010; Rao *et al.* 2011).

It may be recalled that the critical parameters for transition are sensitive to the placement of boundaries and the resolution of the wake. In order to reduce blockage effects to acceptable levels, the boundaries of the domain have been placed at $100D$ from the cylinder in all directions.

3.2. *Linear stability analysis*

The focus of this investigation is to determine the three-dimensional stability of the two-dimensional base flows to perturbations with an imposed spanwise wavelength.

Equations for the evolution of perturbations are formed by first decomposing the velocity and pressure fields into base and perturbation components. This decomposition is then substituted into the governing Navier–Stokes equations, and the terms for the base flow subtracted out. The resulting equations are then linearized by removing the quadratic perturbation term. Because the coefficients do not depend on z, the perturbation fields can be decomposed into a set of Fourier modes in the spanwise direction, and the perturbation equations then reduce to a set of decoupled equations describing the different spanwise modes. The process of forming these equations is well described in Barkley & Henderson (1996). The result is that perturbation fields for an imposed spanwise wavelength can be solved for.

The eventual perturbation equations can be viewed as a linear operator that takes the perturbation solution from one time to another. If the base flow is periodic, this results in an operator that takes the perturbation from one period to the next. This operator is never explicitly formed; application of the operator is obtained by simply integrating the perturbation equations forward in time. Eigenvalues μ of this operator indicate whether the base flow is steady to perturbations of a prescribed wavelength: $|\mu| < 1$ indicates that the flow is stable as perturbations decrease in size from one period to the next; $|\mu| > 1$ indicates that the base flow is unstable as perturbations grow from one period to the next. For periodic problems, μ is referred to as the Floquet multiplier. Marginal stability occurs when $|\mu| = 1$.

Of interest are the eigenmodes (Floquet modes or linear instability modes) with the largest eigenvalues, as these are the modes which grow the fastest (or decay the slowest). As the linear operator is never explicitly formed, these leading eigenmodes and eigenvalues are found through indirect iterative methods. Here, an Arnoldi method is employed (e.g. Mamun & Tuckerman 1995) that can resolve the leading eigenmodes and the complex component of the eigenvalues of μ. When μ is purely real and positive, the periodicity of the three-dimensional mode is synchronous with the base flow; e.g. modes A and B, which are observed in the wake of a non-rotating cylinder, are purely real modes (Barkley & Henderson 1996). When μ is complex, the eigenmode introduces a new frequency. If the base flow is steady, this predicts that the three-dimensional flow will be periodic; if the base flow is periodic, the introduction of this second frequency predicts that the three-dimensional flow will be quasi-periodic. Finally, if the Floquet multiplier is purely real but negative, subharmonic modes are predicted. Further details of this method and its implementation can be found in Leontini *et al.* (2007) and Stewart *et al.* (2010).

Linear stability analysis has been widely used to predict critical Reynolds numbers and wavelengths of three-dimensional modes that become unstable based on a periodic or steady two-dimensional base flow. The spatial structure of the modes is also predicted. For a non-rotating cylinder, the predictions of the linear (Floquet) instability modes (modes A and B) by Barkley & Henderson (1996) agree well with the fully saturated instability modes observed in the experiments of Williamson (1988), both in terms of the observed wavelengths and spatio-temporal symmetries. In terms of the general mode structure, the fully saturated mode A structure appears to maintain a higher amplitude further downstream relative to the linear mode, but the overall mode structure is similar, especially near the cylinder. Naturally, the fully saturated mode states are of interest since the existence of one mode may alter the occurrence or onset of another mode. For example, in practice, mode B becomes unstable at a lower Reynolds number ($Re \sim 230$–240) than predicted by the Floquet stability analysis based on the two-dimensional periodic base flow ($Re = 260$), while mode A is also
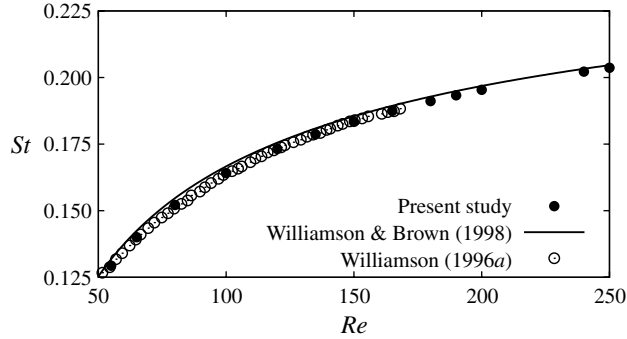
FIGURE 2. Verification of the spectral-element code and the domain used. Comparisons with previous results of the vortex shedding frequency for a fixed cylinder in two-dimensional flow. The solid line is the three-term fit for *St*–*Re* variation below *Re* < 1000 from Williamson & Brown (1998).

found to become chaotic in its fully saturated state (Williamson 1988). These issues require analysis using direct numerical simulations and experiments, and are beyond the scope of this paper.

3.3. *Comparisons with previous studies*

Shown in figure 2 is a comparison of the Strouhal number *St* variation with *Re* for the non-rotating cylinder in a free stream, with values of *St* from the current study and those from Williamson (1996a). Here, $St = fD/U$, where f is the frequency of vortex shedding. The comparison is excellent. The solid line in the figure is from the three-term fit by Williamson & Brown (1998), where *St* is given by

$$St = \left(0.2731 - \frac{1.1129}{\sqrt{Re}} + \frac{0.4821}{Re} \right). \tag{3.1}$$

Spatial resolution studies were carried out for the rotating cylinder at $\alpha = 2$ and $Re = 400$ to investigate the accuracy of the predictions. This study was performed at the highest rotation rate for which the unsteady flow was observed. The solutions at $N \times N = 49$ converge to within 0.2 % of the maximum tested resolution at $N \times N = 81$. Furthermore, the values of the time-averaged force coefficients for a resolution of $N \times N = 36$ are well within 1 % of the maximum tested values. A resolution of $N \times N = 49$ was therefore determined to be sufficient to capture the forces accurately up to $\alpha \leqslant 2.5$; however a resolution of $N \times N = 64$ was used to accurately capture the forces for all rotation rates beyond $\alpha > 2$. Shown in figure 3 is a comparison of the variation of time-averaged lift and drag coefficients with rotation rate. Shown in figure 4 is the variation of *St* on increasing the number of internal node points. The figures show that the selected resolution is adequate to resolve the flow accurately.

A linear stability analysis validation study was also performed for the non-rotating cylinder at $Re = 280$, and the growth rates obtained were compared with the results of Barkley & Henderson (1996). The growth rates of the two primary modes (modes A and B) from Barkley & Henderson (1996) match closely with the results of the present study, as shown in figure 5. The very slight differences can be attributed to difference between the domain sizes of the computational domains used.
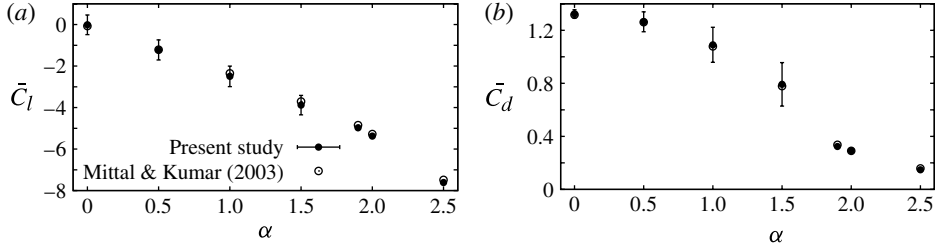
FIGURE 3. Comparison of the time-averaged force coefficients with the results from Mittal & Kumar (2003). Variation of the time-averaged (*a*) lift coefficient, $\bar{C}_l$, and (*b*) drag coefficient, $\bar{C}_d$. The vertical error bars represent one standard deviation of the instantaneous force coefficients.
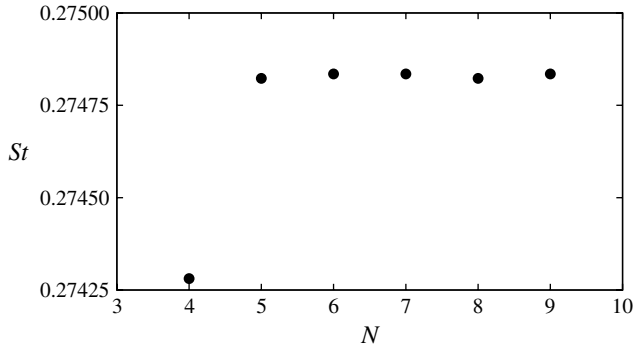

FIGURE 4. Spatial resolution study at $\alpha = 2$ and $Re = 400$. Variation of the shedding frequency (*St*) with increasing internal node points (*N*) is shown.

4. Flow structures

Over the range of the parameters tested, three two-dimensional flow regimes have been identified. Instantaneous snapshots of vorticity providing examples of each of these regimes are presented in figure 6, all at $\alpha = 1.9$. Shown are the steady regime (figure 6*a,b,d*), the low-frequency regime (figure 6*c,g,h*) and the high-frequency regime (figure 6*e,f*). As for the limiting case of a stationary cylinder, at low Reynolds numbers the flow is steady. For $\alpha \lesssim 1.95$, periodic vortex shedding is found to occur above a critical Reynolds number, which is a function of α. For $\alpha \gtrsim 1.95$, the two-dimensional flow was found to remain steady up to at least $Re = 400$.

However, as the sequence of images of figure 6 shows, increases in Re restabilize the two-dimensional flow, for a narrow band of α centred around $\alpha = 1.9$. This indicates that the value of Re at the steady–unsteady transition is not a monotonic function of α. This finding is further expanded upon in § 5.

The periodic vortex shedding can be further divided into two regimes, based upon the frequency of the oscillation. The variation of the shedding frequency as a function of Re, for $1.8 \leqslant \alpha \leqslant 2.0$, is shown in figure 7. Clearly discernible is the development of two 'branches', with a 'high'-frequency and 'low'-frequency branch appearing for $Re \geqslant 260$. At $\alpha = 1.8$, the *St–Re* curve is continuous. For $\alpha \geqslant 1.9$, the behaviour is much more complex. Taking $\alpha = 1.9$ as an example, for $Re < 190$, the frequency

of oscillation remains on the low-frequency branch. For $190 < Re < 260$, the flow is stabilized, and no vortex shedding occurs (figure 6*d*). Then for $260 \lesssim Re \lesssim 340$, the vortex shedding moves to the high-frequency branch (figure 6*e*), before dropping back again to the low-frequency branch for $Re > 340$ (figure 6*h*).

Shown in figure 8 are force-coefficient phase diagrams for $\alpha = 1.9$ at the specified Reynolds numbers. The variation of the drag coefficient with lift coefficient is shown over one complete period of shedding. The flow states in the steady regimes are represented by singular points, while those in the periodic states are characterized by closed orbits. These phase diagrams also provide an indication of the amplitude of shedding. The amplitude of force (and wake) oscillations is small at low Reynolds numbers, and remains so on the 'high'-frequency branch. In comparison, larger amplitudes are observed at high Reynolds numbers, when the flow returns to the 'low'-frequency branch.

5. Stability analysis

The results presented in §4 show that, over the parameter space investigated, all of the two-dimensional flows are either steady or periodic. This means that all are amenable to either linear stability analysis (for the steady flows) or Floquet stability analysis (for the periodic flows). In fact, the two techniques are effectively identical in practice, if the steady flow is treated as a flow with arbitrary period. Stability analysis was performed on the flows over the parameter space ($Re \leqslant 350$, $0 \leqslant \alpha \leqslant 2.5$) to determine the critical transitional values for the onset of a number of three-dimensional modes, which govern the transition to three-dimensional flow.

For the limiting case of a non-rotating cylinder ($\alpha = 0$), the transition to three-dimensionality has been well documented by various numerical studies (Barkley & Henderson 1996; Thompson *et al.* 1996) and is found to occur at $Re = 188.5 \pm 1$ for a spanwise wavelength of $\lambda/D = 3.96$. For a cylinder rotating at $\alpha = 0.5$, a more recent study by Akoury *et al.* (2008) found the critical value of transition to three-dimensionality to occur at $Re = 220$. They report that the wake structure was similar to the mode A structure obtained for the flow past a non-rotating cylinder, and it remained unchanged at $Re = 300$. At much higher rotation rates of $\alpha = 5$, and at $Re = 200$, the primary cause of three-dimensionality has been attributed to centrifugal instabilities (Mittal 2004). The variation of the critical Reynolds number at other rotation rates has not been investigated. Therefore, a systematic study of the three-dimensional modes present in the (Re,α) plane is presented in §5.1.

5.1. *Transition diagram*

Figure 9(*a*) shows curves of marginal stability for seven separate three-dimensional modes growing on the two-dimensional base flows outlined in §4. Also shown is the boundary for the steady–unsteady transition. The results compare well with the predictions of Pralits *et al.* (2010) for $\alpha \leqslant 2$. The points on each of the curves denote a point at which the marginal stability of the mode in question has been established; the curves have then been fitted to these points. As the majority of the modes' marginal stability curves occur in the top-right corner of the figure, an enlarged version of this region is presented in figure 9(*b*). These curves have been found by first resolving the two-dimensional flows over a grid of points in the (Re, α) plane, then performing the stability analysis over a spectrum of wavelengths at each of these points, and then refining this grid in the region of marginal stability for each

mode. This process was very computationally intensive; the data for the current study consumed the order of 10^5 CPU hours.

There are a number of features of figure 9 that are examined in some detail in the following sections. First, the variation of the steady–unsteady transition is described. Following this, descriptions of each of the three-dimensional modes are presented, including the mode structure, critical wavelengths, spatio-temporal symmetries, and some further analysis and interpretation of the physical mechanisms of instability.

5.2. *The steady–unsteady transition*

For lower rotation rates ($\alpha \leqslant 1$), the transition to the unsteady regime occurs at a value of Re close to that of the non-rotating cylinder. However, for $\alpha \gtrsim 1.3$, small changes in the rotation rate rapidly shift the transition to higher Reynolds numbers. For $\alpha \geqslant 2.1$, the two-dimensional base flow is seen to remain steady up to at least $Re = 400$.

As was shown in figure 6, for a small band of α centred around $\alpha = 1.9$, further increases in Re can restabilize the flow. This is shown particularly clearly in figure 9(*b*), where the solid line marking this transition is shown to descend over the range $180 < Re \lesssim 220$, and then ascend for $Re \gtrsim 220$. The cause of this complicated behaviour is not clear. The onset of the high-frequency regime shown in figure 7 roughly coincides with the point at which the curve begins to ascend; it is therefore possible that this high-frequency regime is due to an instability of the stabilized flow; however further work is required to fully understand this phenomenon.

5.3. *Properties of the three-dimensional modes*

5.3.1. *The mode A instability*

For a non-rotating cylinder in a free stream, the onset of three-dimensional flow is observed around $Re = 180$ in experiments, with a spanwise wavelength of approximately 4*D* (Williamson 1996*b*). This same mode has been observed numerically by the three-dimensional simulations of Thompson *et al.* (1996), and the linear stability analysis (Barkley & Henderson 1996) explained the basis of the transition. This mode is referred to as mode A and for a non-rotating cylinder has been shown to be the fastest-growing linear mode up to $Re = 280$ (also see figure 5). The physical mechanism of this mode has been associated with an elliptic instability of the forming vortex cores (Leweke & Williamson 1998; Thompson, Leweke & Williamson 2001).

From the stability analysis of this paper, mode A is found to persist for $\alpha \leqslant 1.9$, over the entire range where the two-dimensional base flow is unsteady. As shown in figure 9, the critical Reynolds number with respect to the marginal stability of mode A is a strong function of α. For $\alpha \leqslant 1.25$, the critical Reynolds number increases on increasing the rotation rate. Over this range, mode A is also the first mode that occurs with increasing Re, and so will lead the transition to three-dimensionality. The Floquet multiplier obtained is positive and real.

Previous studies using fully three-dimensional direct numerical simulations (DNS) (Akoury *et al.* 2008) have found that, for $\alpha = 0.5$, the critical Reynolds number for the transition to three-dimensional flow occurred at $Re \simeq 220$. This result matches well with the curve of marginal stability for mode A in figure 9(*a*).

The critical wavelength at the onset of this instability was approximately 4*D*. At a higher rotation rate of $\alpha = 1.5$, the transition occurs at $Re_c \simeq 288$, and occurs at higher Reynolds numbers as the rotation rate is increased (figure 9).

Figure 10(*a–c*) shows the spanwise perturbation vorticity contours in two dimensions just beyond the critical Reynolds number for a series of rotation rates.
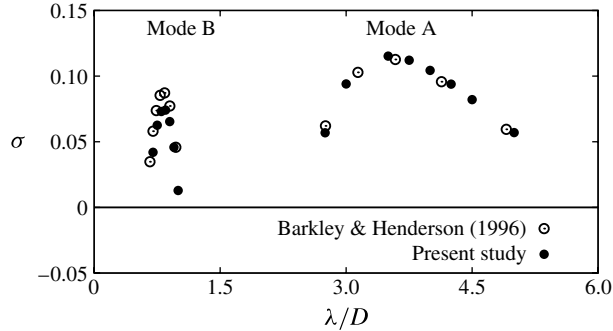
FIGURE 5. Validation of the stability analysis at higher Reynolds numbers for a non-rotating cylinder: comparison of the growth rate at different spanwise wavelengths at $Re = 280$ between results from Barkley & Henderson (1996), and from the present study. The neutral stability line at $\sigma = 0$ is marked by a solid line.
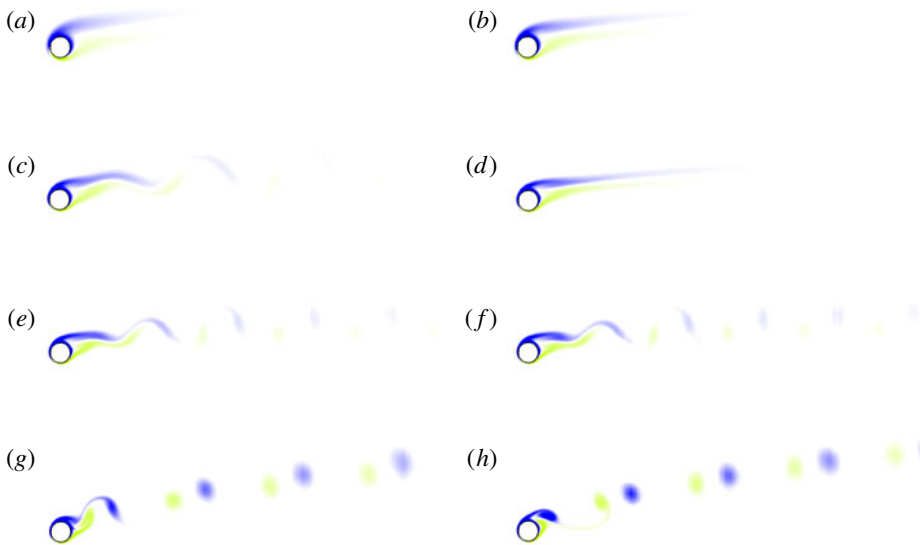

FIGURE 6. (Colour online) Flow structures at $\alpha = 1.9$ at Reynolds numbers: (*a*) $Re = 50$; (*b*) $Re = 100$; (*c*) $Re = 180$; (*d*) $Re = 250$; (*e*) $Re = 325$; (*f*) $Re = 340$; (*g*) $Re = 350$; (*h*) $Re = 400$. Vorticity contour levels between $\pm 5D/U$. The flow is from left to right.

These images are all shown at a similar phase in the vortex shedding process. The spatial structure of this mode is preserved at higher rotation rates, regardless of the fact that the vortex shedding becomes increasingly asymmetric about the centreline with increasing α. The shaded region in figure 10(*d*) shows the occurrence of the mode A instability in the parameter space. A three-dimensional reconstruction of the spanwise perturbation vorticity contours is shown in figure 10(*e*). The perturbation field was added to the two-dimensional base flow to obtain these images in a perspective view. The perturbation isosurfaces (red (dark grey) and yellow (light grey)) are visualized for the cylinder spinning at $\alpha = 1$ at $Re = 280$. Two spanwise wavelengths are shown.
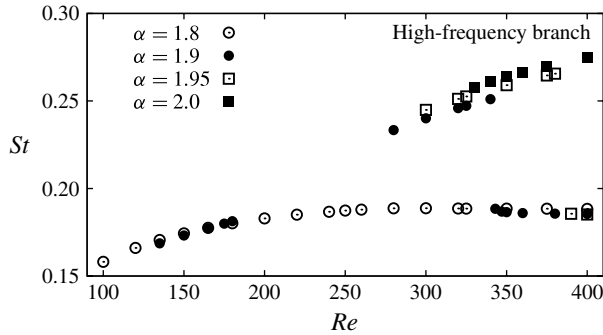
FIGURE 7. Variation of the shedding frequency with Reynolds number for the specified rotation rates. For $\alpha \geqslant 1.9$, two branches or regimes of shedding occur.
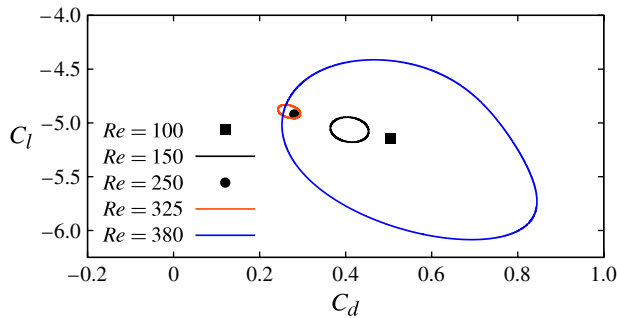

FIGURE 8. (Colour online) Phase diagrams of the force coefficients at the specified Reynolds numbers for $\alpha = 1.9$.

5.3.2. *The mode B instability*

For a non-rotating cylinder, mode B is observed to become unstable at Reynolds numbers higher than that observed for mode A. In the experimental visualizations of Williamson (1988), this mode was observed intermittently alongside mode A for $Re \simeq 230$ with a spanwise wavelength of approximately $1D$. The numerical simulations of Barkley & Henderson (1996) predicted the onset of this linear mode from the two-dimensional base flow at $Re = 259$ with a spanwise wavelength of $\lambda \simeq 0.8D$. The contrast to the experimental findings is due to the fact, in experiments, the flow is already three-dimensional due to the presence of mode A. Barkley, Tuckerman & Golubitsky (2000) showed that the presence of mode A is destabilizing for the mode B instability, leading to mode B occurring at lower Reynolds numbers in experiments. The linear mode associated with mode B is the fastest growing mode for $Re > 300$ (Barkley & Henderson 1996; Blackburn *et al.* 2005) for the non-rotating cylinder.

The simulations of this paper recover mode B, and show that it continues to exist up to at least $\alpha = 1$. Similar to the non-rotating cylinder, the Floquet multiplier for this mode remains purely real and positive. As shown on figure 9(*a*), the value or Re at marginal stability is a strong function of α, increasing as α is increased. However, the characteristic wavelength is relatively unaffected by α, remaining close to $\lambda = 0.8D$. Over the range of the parameter space tested, mode B is always found to become unstable at Re higher than that at which mode A becomes unstable.
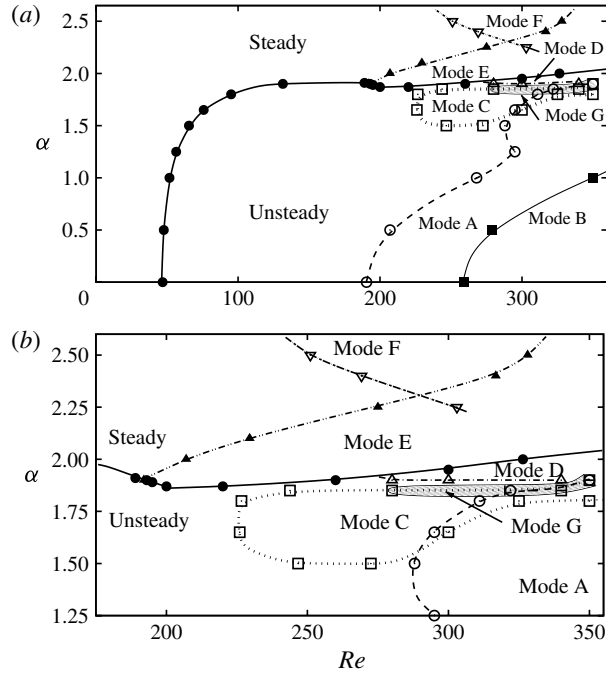
FIGURE 9. (*a*) Diagram showing the lines of marginal stability in the parameter space investigated. (*b*) Enlarged view of (*a*) between $1.25 \leqslant \alpha \leqslant 2.5$, $175 \leqslant Re \leqslant 350$. In both images, the steady–unsteady transition is shown by a continuous line, while the boundaries of the stability of the three-dimensional modes are shown by broken lines. To further differentiate the modes, the following symbols have been used. $\bigcirc$, Mode A; $\blacksquare$, Mode B; $\square$, Mode C; $\triangle$, Mode D; $\blacktriangle$, Mode E; and $\triangledown$, Mode F. Mode G occurs over a narrow region and is represented as a shaded region.

Figure 11 shows the perturbation vorticity contours of mode B at rotation rates of $\alpha = 0$, 0.5 and 1. Note that for the case at $\alpha = 0.5$ (figure 11*b*), the base flow is approximately half a period out of phase with respect to the other images; however the similarity in the structure of the mode is evident. For all α, the perturbations grow strongly in the braid regions between the shed vortices, similar to what is observed for a non-rotating cylinder (shown as $\alpha = 0$ in figure 11*a*). The occurrence of the mode B instability in the parameter space is shown by the shaded region in figure 11(*d*) and the three-dimensional reconstruction of the perturbation field in figure 11(*c*) is shown in figure 11(*e*).

5.3.3. *The mode C instability*

The previous modes described, A and B, are basically extensions of the modes found in the wake of a non-rotating cylinder. However, there are a number of other modes presented on figure 9 that occur only for the rotating cylinder. The first of these is mode C.

The mode C instability occurs in an apparently closed region of the (Re, α) plane, centred around $Re = 260$, $\alpha = 1.7$. The Floquet multiplier for mode C is purely real but negative, indicating that this mode is subharmonic, repeating over two cycles of the base flow. The critical spanwise wavelength for this mode is marginally
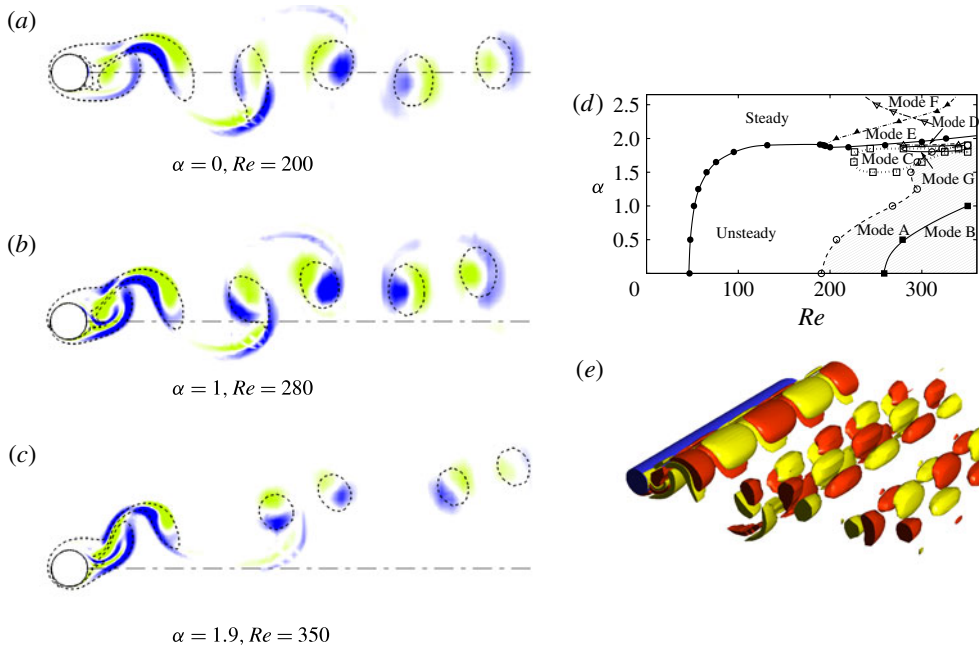
FIGURE 10. (Colour online) (*a–c*) Spanwise perturbation vorticity contours of mode A in the wake of the rotating cylinder between levels $\pm 0.1 U/D$ at the specified rotation rates and Reynolds numbers, for a spanwise wavelength of $\lambda/D = 4$, at an arbitrary time in the shedding cycle. Base-flow vorticity contours at levels $\pm 1 U/D$ are overlaid as dashed lines. A centreline line is drawn in the streamwise direction behind the cylinder. (*d*) The occurrence of the mode A instability in the parameter space is highlighted in the parameter space diagram. (*e*) Perspective view showing the isosurfaces of the spanwise perturbation vorticity contours (in red (dark) and yellow (light grey)) of the mode A instability shown in (*b*). Two spanwise wavelengths are shown. Flow is from left to right in all images.

higher than for mode B, but lower than for mode A, and encompasses the range $0.8 < \lambda_c/D < 1.2$.

The group-theory analysis of the symmetries of bluff-body wakes of Blackburn *et al.* (2005) shows that for flows with the spatio-temporal symmetry of the wake of a non-rotating cylinder (reflection about the wake centreline plus evolution in time of half a period), subharmonic instabilities are not generic, and are therefore not likely to be discovered. However, once this spatio-temporal symmetry is broken, subharmonic modes become possible. Here, the spatio-temporal symmetry is broken by the rotation of the cylinder, hence the presence of the subharmonic mode C. In structure, mode C appears very similar to the subharmonic mode C found in the wakes behind rings (Sheard *et al.* 2003, 2005*a*,*b*). In both of these flows, the symmetry is broken by a local acceleration of the flow on one side of the body; here the acceleration is due to the rotation of the cylinder, in ring wakes it is caused by the acceleration of the flow through the constriction of the centre of the ring. Similar subharmonic modes have be found in other wake flows, such as cylinders with trip wires (Zhang *et al.* 1995), and in the wakes of transversely oscillating cylinders after undergoing spontaneous transition to a $P + S$ base state (Leontini *et al.* 2007), and more recently in the wakes of inclined square cylinders (Sheard *et al.* 2009; Sheard 2011).
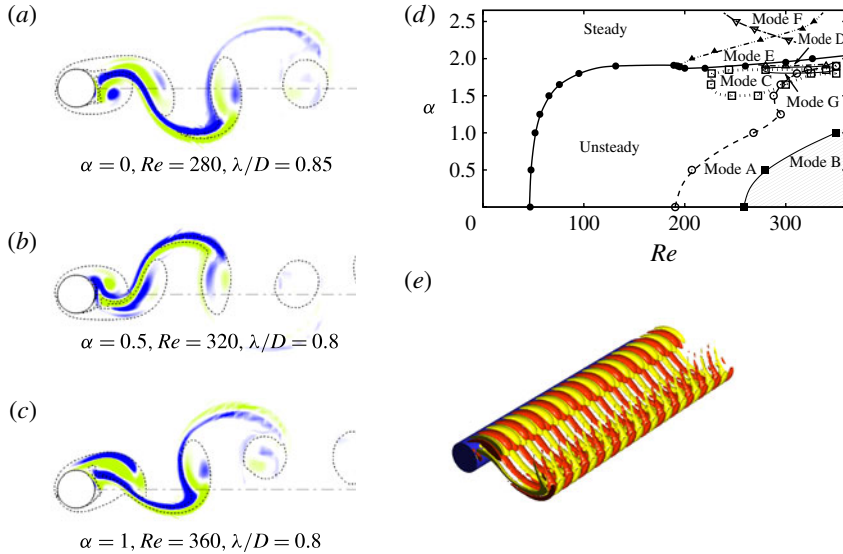
(a) $\alpha = 0, Re = 280, \lambda/D = 0.85$

(b) $\alpha = 0.5, Re = 320, \lambda/D = 0.8$

(c) $\alpha = 1, Re = 360, \lambda/D = 0.8$

FIGURE 11. (Colour online) (*a–c*) Spanwise perturbation vorticity contours of mode B in the wake of the rotating cylinder between levels $\pm 0.1 U/D$ at the specified rotation rates and Reynolds number at an arbitrary time in the shedding cycle. Base-flow vorticity contours at levels $\pm 1 U/D$ are overlaid as dashed lines. A centreline line is drawn in the streamwise direction behind the cylinder. (*d*) The occurrence of the mode B instability in the parameter space is highlighted by the shaded region. (*e*) A three-dimensional reconstruction of the spanwise perturbation vorticity contours of (*c*) over a spanwise distance $z/D = 9.6$. Flow is from left to right in all images.

Shown in figure 12 are the perturbation vorticity contours of the mode C instability at $\alpha = 1.5$, $Re = 250$. The perturbation field reverses in sign every period, indicating that this mode is periodic over $2T$, where T is the period of the two-dimensional periodic base flow. Figure 12(*a–f*) shows the spanwise perturbation field over a period $2.5T$. The occurrence of the mode C instability is shown by the shaded region in figure 12(*g*). The three-dimensional reconstruction of this mode is shown in figure 12(*h*) over a spanwise distance of $z/D = 9.6$.

The growth rates of mode C are highest in the centre of the region over which it is unstable. Unlike mode A or mode B, the magnitude of the Floquet multiplier does not show a monotonic increase with rotation rate. Shown in figure 13 are the variation of growth rate at constant rotation rate (figure 13*a*), and at a constant Reynolds number (figure 13*b*). These values have been chosen to traverse the region where mode C is unstable. The figure shows that the maximum amplification of this mode occurs at $(Re, \alpha) \simeq (260, 1.80)$.

5.3.4. *The mode D instability*

The mode D instability develops on the unsteady base flow, becoming unstable in a narrow region of the parameter space, for values of α just below those at which the base flow is stabilized, as shown on figure 9. The Floquet multiplier for this mode is real and positive. The mode grows with a characteristic spanwise wavelength of approximately $2D$.

Of particular interest is the region of occurrence of this instability; it occurs in essentially the same region of the parameter space as the high-frequency shedding
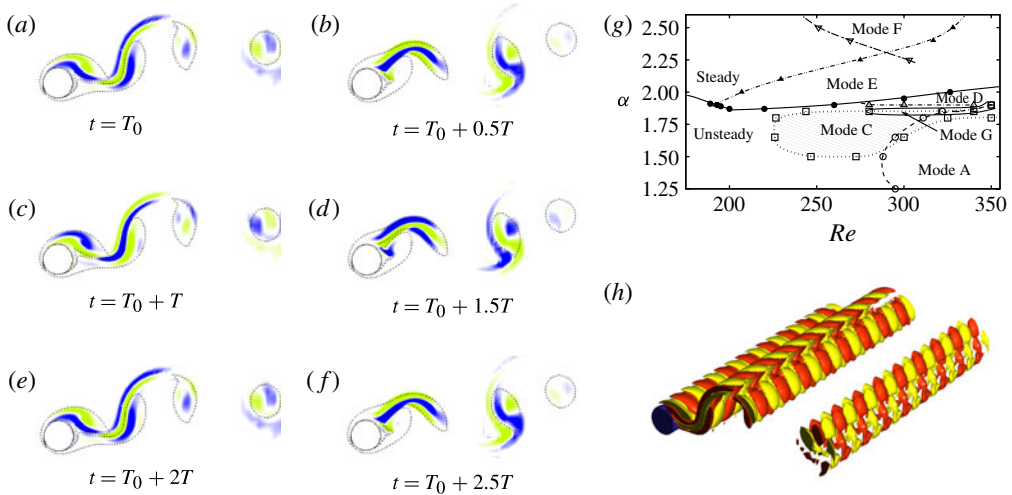
FIGURE 12. (Colour online) (*a–f*) Spanwise perturbation vorticity contours of mode C at $\alpha = 1.5$, $Re = 250$, $\lambda/D = 1.2$ between levels $\pm 0.1 U/D$ over a period of 2.5T. Base-flow vorticity contours at levels $\pm 1 U/D$ are overlaid as dashed lines. The perturbation vorticity contours are identical after two periods of the base flow. (*g*) The occurrence of the mode C instability in the parameter space is highlighted by the shaded region. (*h*) A three-dimensional rendering of the spanwise perturbation vorticity contours of the mode C instability over a spanwise distance $z/D = 9.6$. Flow is from left to right in all images.
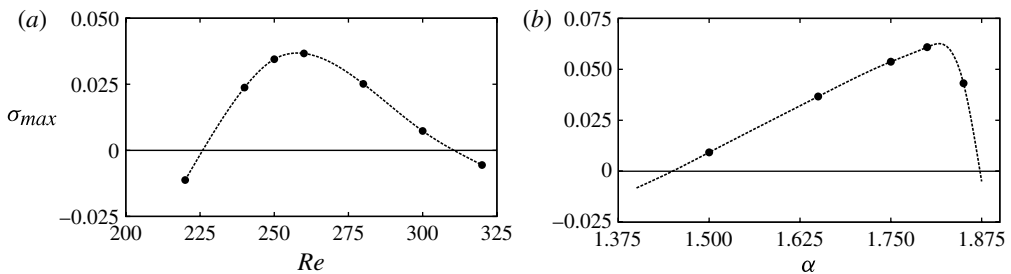

FIGURE 13. Variation of the maximum growth rate (σ_{max}) with respect to wavelength (λ/D), for the mode C instability: (*a*) at constant rotation rate of $\alpha = 1.65$; and (*b*) constant Reynolds number $Re = 260$. These indicate the closed region of instability for mode C.

regime (figures 7 and 9). This high-frequency shedding regime consists of two highly strained vortices trailing the cylinder, and small vortices are emitted from the end of these (see, for example, figure 6).

This instability grows in the region between these two strained vortices. Shown in figure 14(*a,b*) are the spanwise and streamwise perturbation vorticity contours at $\alpha = 1.9$ and $Re = 300$. This structure is very similar to mode E, described next, which grows on the steady base flow. In particular, disregarding the steady or unsteady nature of the base flow, the perturbation field structures appear similar. It is therefore hypothesized that modes D and E occur due to the same physical instability mechanism. The occurrence of the mode D instability is shown by the shaded region
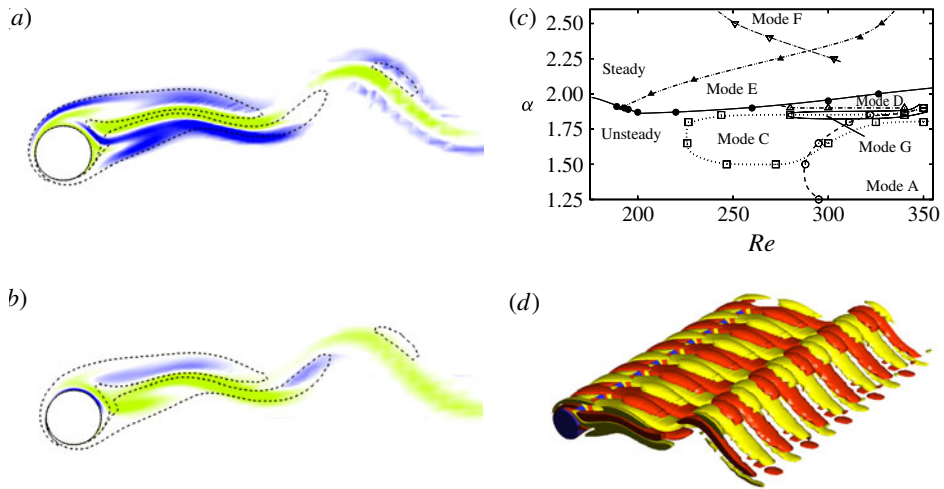
FIGURE 14. (Colour online) Perturbation vorticity contours in the wake of the rotating cylinder at $\alpha = 1.9$, $Re = 300$, $\lambda/D = 1.9$, highlighting the perturbation field structure for Mode D: (*a*) spanwise vorticity, (*b*) streamwise vorticity. The perturbation contour levels are between $0.1U/D$ with the base-flow vorticity contours at levels $\pm 1U/D$ overlaid as dashed lines. (*c*) The occurrence of the mode D instability in the parameter space is highlighted by the shaded region. (*d*) A three-dimensional rendering of the perturbation vorticity contours of the mode D instability over a spanwise distance $z/D = 9.6$. Flow is from left to right in all images.

in figure 14(*c*) and the three-dimensional reconstruction of the perturbation field is shown in figure 14(*d*).

5.3.5. *The mode E instability*

The first three-dimensional mode to become unstable as α is increased on the steady base flow is mode E. The multipliers, or growth rates, for this mode are purely real, indicating that when this mode becomes unstable, it triggers a transition from a two-dimensional steady state to a three-dimensional steady state. The characteristic wavelength for this mode is approximately $2D$, again consistent with mode D. The spanwise wavelength at which the maximum growth rate occurs decreases as the Reynolds number is increased.

Shown in figure 15(*a,b*) are the spanwise and streamwise perturbation vorticity contours for $\alpha = 2$ and $Re = 220$, showing an example of the mode E instability. The occurrence of this mode is shown by the shaded region in the parameter space (figure 15*c*). As already discussed above, this mode has similar characteristics to those of the mode D instability. The regions of high perturbation amplitude are similar to those of mode D in the near wake, while the instability extends in the flattened wake far downstream of the cylinder, which is more evident in the three-dimensional reconstruction of the perturbation field (figure 15*d*).

5.3.6. *Physical nature of the mode D and E instability*

Figure 16 shows the spanwise and streamwise perturbation vorticity as colour contours, overlaid with the streamlines of the base flow, for $\alpha = 2$, $Re = 220$. The base-flow vorticity contours of figure 15 for the same case show regions of positive and negative vorticity in the wake. However, the streamlines of figure 16 show that only a single recirculation region exists.
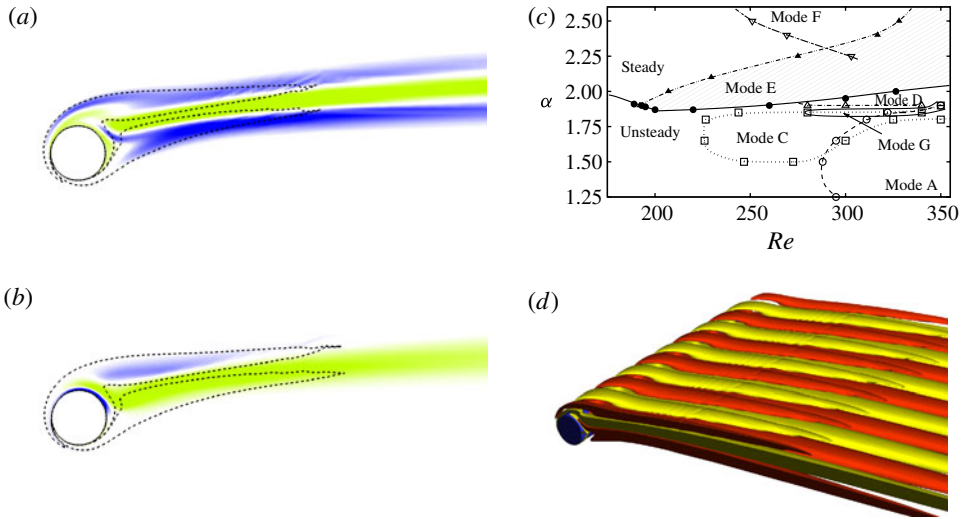
FIGURE 15. (Colour online) Perturbation vorticity contours in the wake of the rotating cylinder for mode E at $\alpha = 2$, $Re = 220$, $\lambda/D = 2.0$: (*a*) spanwise vorticity, (*b*) streamwise vorticity. The perturbation contour levels are between $0.1 U/D$ with the base-flow vorticity contours at levels $\pm 1U/D$ overlaid as dashed lines. (*c*) The occurrence of the mode E instability in the parameter space is highlighted by the shaded region. (*d*) A three-dimensional rendering of the perturbation vorticity contours of the mode E instability over a spanwise distance $z/D = 9.6$. Flow is from left to right in all images.
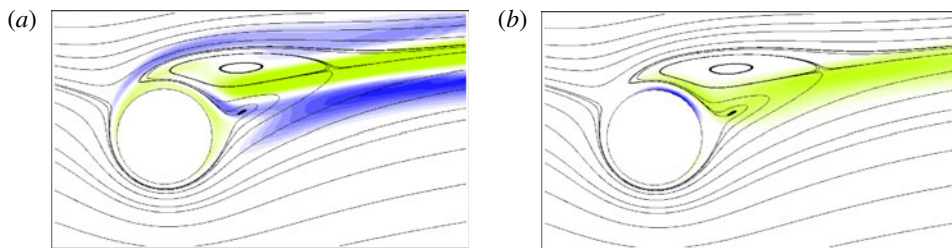

FIGURE 16. (Colour online) Perturbation vorticity contours, overlaid with streamlines, in the wake of the rotating cylinder for mode E at $\alpha = 2$, $Re = 220$, $\lambda/D = 2.0$: (*a*) spanwise vorticity, (*b*) streamwise vorticity. Contours range between ± 0.6 for spanwise vorticity, ± 0.4 for streamwise vorticity. The figure shows that the mode is focused in the extensional regions emanating from the hyperbolic point at the rear of the recirculation region.

Figure 16 shows that the perturbation vorticity is mostly focused in a thin region emanating both upstream and downstream of the hyperbolic stagnation point at the rear of this recirculation region. This region of the base flow is characterized by a stretching in the flow direction (along the streamlines); fluid particles increase in speed as they leave the hyperbolic point in this direction. Lagnado, Phan-Thien & Leal (1983) showed, in an inviscid setting, that simple extensional flows lead to an amplification of perturbation vorticity. Leblanc & Godeferd (1999) showed that in Taylor–Green cells (a square geometry containing four rotating cells of fluid, creating a hyperbolic point at the centre), the perturbation vorticity was most amplified along
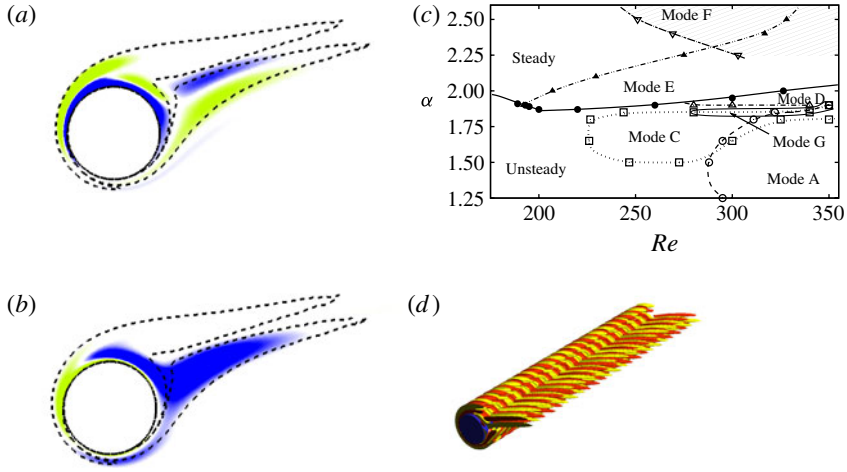
FIGURE 17. (Colour online) Perturbation vorticity contours in the wake of the rotating cylinder for mode F at $\alpha = 2.5$, $Re = 280$, $\lambda/D = 0.45$: (*a*) spanwise vorticity, (*b*) streamwise vorticity. The perturbation contour levels are between $0.1U/D$ with the base-flow vorticity contours at levels $\pm 1U/D$ overlaid as dashed lines. (*c*) The occurrence of the mode F instability in the parameter space is highlighted by the shaded region. (*d*) A three-dimensional rendering of the perturbation vorticity contours of the mode F instability over a spanwise distance $z/D = 9.6$. Flow is from left to right in all images.

the streamlines leaving the hyperbolic point, forming rib vortices in between the rotating cells. A similar amplification mechanism has been proposed by Leweke & Williamson (1998) as the cause of the mode B instability.

Owing to the clear amplification of perturbation vorticity along the streamlines leaving the hyperbolic point in figure 16, it is therefore proposed that this is the amplification mechanism that leads to mode E becoming unstable. The similarity in structure of the perturbation vorticity for modes D and E (albeit that mode D is periodic, with vortex shedding occurring downstream of the recirculation region as shown in figure 14) suggests that it is this same stretching mechanism that leads to the instability of mode D.

5.3.7. *The mode F instability*

A second three-dimensional mode is found to grow on the steady base flow, designated as mode F. This mode typically occurs at higher rotation rates ($\alpha \geqslant 2.25$) than mode E. The characteristic wavelength of this mode is approximately $0.45D$, much shorter than mode E which grows in region between the highly strained standing vortices in the wake.

Shown in figure 17(*a*,*b*) are the spanwise and streamwise vorticity contours at $\alpha = 2.5$ and $Re = 280$. The figure shows that mode F grows primarily in the boundary layer of the spinning cylinder, and in the near wake. Figure 17(*c*) shows the occurrence of the mode F instability in the parameter space. The three-dimensional reconstruction of the mode F instability is shown in figure 17(*d*) over a spanwise distance of $z/D = 9.6$.

The Floquet multipliers for this mode occur in complex-conjugate pairs. This indicates that while the two-dimensional base flow is steady, transition to this mode marks a transition to three-dimensional flow and the onset of time dependence.
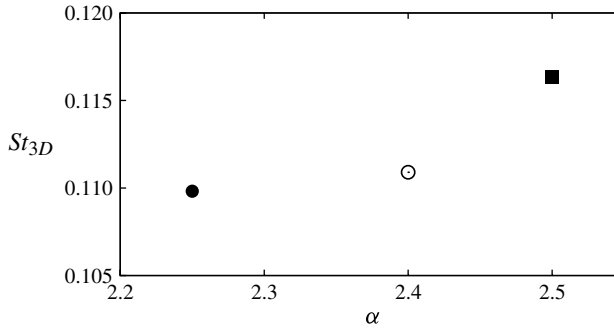
FIGURE 18. Variation of St_{3D} for the three rotation rates ($\bullet$, $\alpha = 2.25$; $\circ$, 2.4; $\blacksquare$, 2.5) at a Reynolds number just beyond the onset of instability for mode F.

The frequency of this time dependence can be ascertained from the complex component of the Floquet multiplier. This was done for values of $2.25 \leqslant \alpha \leqslant 2.5$ and the results are presented in figure 18. The three-dimensional shedding frequency at the onset of the instability is computed as follows: $St_{3D} = \tan^{-1}(\text{Im}(\mu)/\text{Re}(\mu))/2\pi T$, where St_{3D} is the three-dimensional shedding frequency and T is the period of sampling. This frequency was also determined independently by directly measuring the perturbation-field period to ensure that the choice of T had not caused aliasing to a different frequency. For all rotation rates at which this mode is unstable, the three-dimensional frequencies are low, considerably lower than those of the unsteady two-dimensional base flows at lower values of α. Fully three-dimensional DNS, or experiments, are required to see if this predicted frequency corresponds to that found in the fully saturated three-dimensional flow, and what saturated spatial wake structure this three-dimensional flow will take.

5.3.8. *Physical nature of the mode F instability*

As discussed in the introduction, it has already been speculated that the higher-rotation-rate flows are subject to a centrifugal instability (e.g. Mittal 2004; Meena *et al.* 2011). The generalized centrifugal theory of Bayly (1988) has therefore been applied to investigate the nature of this instability mode. That work extends the classical analysis of Rayleigh (1917) to non-axisymmetric inviscid flows with closed streamlines. More recently it has been applied to analyse the recirculating flow downstream of a bump (Gallaire, Marquille & Ehrenstein 2007) and a semicircular hill (Griffith *et al.* 2007). In addition, there have been extensions of the theory to other cases such as to non-zero azimuthal wavenumbers (Billant & Gallaire 2005), and to rotating systems (Sipp & Jacquin 2000).

Physical evidence of centrifugal instability

Figure 19(*a*) displays streamlines for the mode F base flow for $Re = 280$ and $\alpha = 2.4$. The closed streamlines in the neighbourhood of the surface of the cylinder are clearly apparent. Figure 19(*b*) shows the evolution of the perturbation streamwise vorticity field over one half of a period (the period being $1/St_{3D}$ defined in figure 18). After a half-period the perturbation field is identical but of opposite sign. The period therefore corresponds to the time it takes for a fluid element at the mean radial position of the instability to travel twice around the cylinder, hence in some sense the instability can be considered a subharmonic.
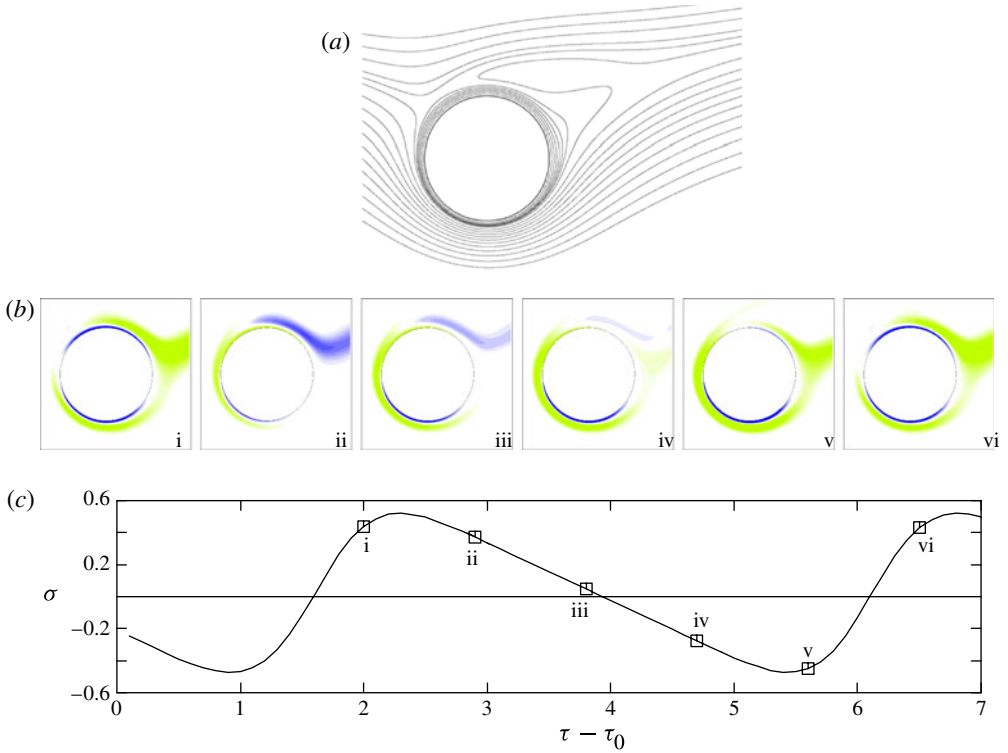
FIGURE 19. (Colour online) Physical evidence of centrifugal instability leading to mode F at $Re = 280$, $\alpha = 2.4$, for a wavelength $\lambda/D = 0.45$. (a) Streamlines of the base flow in the neighbourhood of the cylinder showing that the streamlines are closed in the vicinity of the cylinder. (b) Evolution of the perturbation streamwise vorticity field over half a period: (i) $\tau - \tau_0 = 0T/10$; (ii) $T/10$; (iii) $2T/10$; (iv) $3T/10$; (v) $4T/10$; (vi) $5T/10$; where $\tau = tU/D$, t is time, τ_0 is τ at some arbitrary time and T is the period of the global instability. This progression shows that the period of the instability corresponds to the time taken for the perturbation to orbit the cylinder twice. (c) Instantaneous growth rate of the instability as a function of time. The times/growth rates corresponding to the set of images in (b) are marked.

The development and evolution of the instability involves the development of streamwise perturbation vorticity at the north–west position on the cylinder, approximately at the point where the incoming fluid separates to move either over the top or the bottom of the cylinder. This is shown in figure 19(b i) at $t = 0T/10$. Subsequently, the instability grows as it is advected anticlockwise, following close to the cylinder surface, as shown in the next two images. Figure 19(b iv) shows that some vorticity moves into the wake but some continues along the surface towards the dividing streamline, as shown in figures 19(b v) and 19(b vi). This last image shows that the process starts again, but this time the development begins from vorticity of opposite sign. This image sequence confirms that the perturbation field remains strong predominantly near the cylinder surface, where the streamlines are closed, as would be expected for a centrifugal instability.

Figure 19(c) shows the instantaneous temporal growth rate as the instability evolves. This is obtained directly from integrating the perturbation field over a period and determining the amplitude of the instability field as a function of time. For
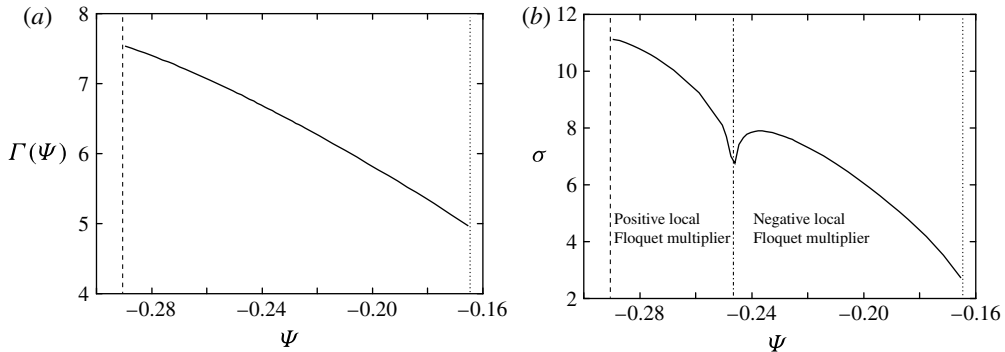
FIGURE 20. (a) Circulation ($\Gamma(\Psi)$) as a function of streamfunction (Ψ) moving from the cylinder surface (dashed line at $\Psi \simeq -0.29$) to the last closed streamline (dotted line). This clearly shows the circulation decreasing outwards as required for centrifugal instability. (b) Magnitude of the growth rate as a function of the streamfunction. The local Floquet multiplier is positive close to the cylinder, but becomes negative further away.

figure 19(b i–iii), growth is positive as the instability advects anticlockwise around the cylinder. For figures 19(b iv) and 19(b v), growth is negative as it traverses across the wake region, before becoming positive again for figure 19(b vi). The Floquet multiplier for a single orbital period of $T = 4.513$ is 1.240, hence the growth rate is $\sigma = \log(1.240)/4.513 = 0.021$.

Application of inviscid centrifugal instability theory

The analysis of Bayly (1988) requires the existence of closed streamlines and the circulation to decrease outwards. Figure 19(a) shows that the condition of closed streamlines is satisfied. Figure 20(a) shows the circulation, $\Gamma(\Psi)$, as a function of the streamfunction (Ψ), moving outwards from the cylinder surface. Clearly, the variation with increasing streamfunction, which also corresponds to increasing radius, is monotonically decreasing. The inviscid analysis of Bayly (1988) is used to determine the eigenvalues of the *local Floquet matrix* on integrating around an entire orbit for each closed streamline. The eigenvalues correspond to local Floquet multipliers, which can be reduced to Floquet exponents, i.e. growth rates, by taking the natural logarithm of the modulus and dividing by the orbital period. Thus the inviscid growth rate (σ_∞) can be determined as a function of streamfunction. Figure 20(b) shows this variation. The local Floquet multiplier is real and positive close to the cylinder, before it becomes real and negative out to the last closed streamline.

Bayly (1988) assumes that the actual instability mode is centred about the quadratic maximum of the growth rate curve, and uses an asymptotic expansion to determine an expression for the growth rate as a function of the wavenumber. In terms of the findings here, there is no quadratic maximum where the Floquet multiplier is positive real, although there is one in the streamfunction range where it is negative real. A negative real Floquet multiplier corresponds to the instability changing sign after each orbit, which figure 19(b) shows is the case here. The actual instability shown in the images of figure 19 is not centred at the streamline position of the streamfunction maximum of figure 20(b), but rather it appears to be centred near the streamline which has an orbital period equal to the measured period of the global instability mode, as would be expected for a centrifugal instability. The value of the streamfunction on this streamline is $\Psi \simeq -0.173$, i.e. close to the outer edge on the recirculation region (see
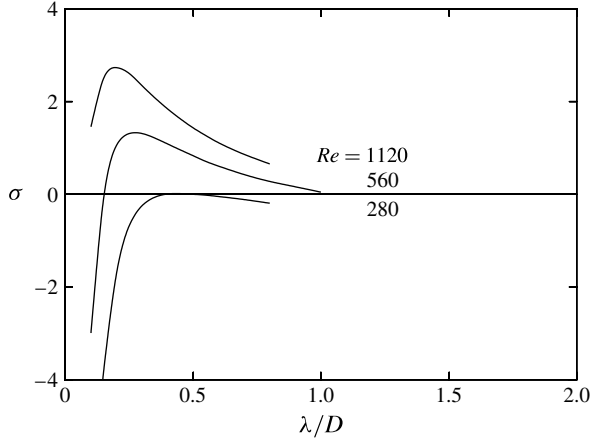
FIGURE 21. Computed growth rate curves as a function of wavelength from global stability analysis. The viscosity (Reynolds number) was varied only for the stability analysis of the base flow at $Re = 280$.

figure 20*b*). The inviscid growth rate is close to $\sigma_\infty \simeq 3.5$ for that trajectory, which represents substantial positive growth.

Expanding about the quadratic maximum indicates that the growth rate should fall off linearly with wavelength (λ) (or inversely with wavenumber (k)) from the inviscid prediction corresponding to the $k \to \infty$ case. Also assuming that the effect of viscosity is mainly to damp the instability rather than change its character, the viscous correction to the growth rate should be proportional to the reciprocal of the square of the wavelength. That is,

$$\sigma(\lambda, Re) \simeq \sigma_\infty - A(\lambda/D) - \frac{4\pi^2 B}{Re\,(\lambda/D)^2}, \tag{5.1}$$

with B a constant of order one. As indicated above, it appears that the instability is not centred about either the absolute maximum or the local quadratic maximum of the inviscid growth curve, but rather about the streamline with the orbital period equal to the global mode period. This is perhaps not surprising given the strong forcing on the fluid from the rapidly spinning cylinder and subsequently stronger viscous effects towards the surface.

To investigate further, the variation of the global mode growth rate with wavelength is plotted in figure 21. The different curves correspond to different Reynolds numbers. The Reynolds number for the steady flow was fixed at 280; it was only varied for the linear stability equations, using the same steady frozen base flow. A similar procedure was used by Gallaire *et al.* (2007) to explore the centrifugal nature of the instability for flow over a bump. According to the proposed variation given by (5.1), the curves should fall inside an envelope curve, with the curves for increasing Reynolds number peaking at progressively smaller wavelengths. The *y* intercept of the envelope curve should correspond to the predicted inviscid growth rate σ_∞. In practice the situation is a little more complex. Increasing the Reynolds number causes the global instability mode to be centred closer to the cylinder and the period to reduce. Table 1 shows this behaviour. Here, λ_{pref} is the wavelength with the maximum growth rate in figure 21, $T_{\lambda_{pref}}$ is half the measured global instability mode period from the global analysis

Re	λ_{pref}	$T_{\lambda_{pref}}$	$\Psi_{\lambda_{pref}}$	$\sigma_{inviscid}$
280	0.44	4.4	-0.172	3.5
560	0.30	3.0	-0.188	5.1
1120	0.22	2.5	-0.201	6.2

TABLE 1. Parameters for global stability analysis based on varying the Reynolds number for the stability equations only.

(recall the mode repeats every two orbits), $\Psi_{\lambda_{pref}}$ is the value of the streamfunction with this orbital period and $\sigma_{inviscid}$ is the predicted growth rate from the inviscid theory of Bayly (1988) shown in figure 20(*b*). In particular, this shows that as the effect of viscosity is reduced, the instability mode moves inwards, centred on streamlines that have smaller orbital periods and higher growth rates, as shown in figure 20(*b*). Thus, it is consistent that the computed growth rate curves shown in figure 21 move upwards, rather than asymptoting to an envelope curve.

Summary of the success of the inviscid theory

   In summary, the mode F instability appears to be associated with a centrifugal instability, in terms of primary localization to the region with both closed streamlines and circulation decreasing outwards. The preferred wavelength of the instability also appears to be related to, i.e. a small multiple of, the radial extent of the region with closed streamlines. In addition, the evolution of the periodic instability mode as it advects around the cylinder is consistent with the formation and growth of streamwise rollers, transferring faster moving fluid to larger radii and vice versa, as expected for a centrifugal instability. This growth happens as the perturbation moves from the dividing streamline at the north–west position of the cylinder until it reaches the wake region at the north–east position on the cylinder, perhaps reminiscent of Görtler vortices (Görtler 1955) for flow on curved streamlines. Analysis using the inviscid instability theory of Bayly (1988) to find the eigenvalues of the local Floquet matrix associated with an orbital period on a streamline predicts substantial amplification during the orbit. There is an inner region where the eigenvalues are positive, and an outer region where they are negative. Negative eigenvalues indicate that the instability changes sign each orbital period. This is precisely what happens with the global mode, i.e. it repeats every two orbits. However, the global mode is not centred close to the streamline at which there is a local maximum of the inviscid growth rate, but rather close to the streamline with the same orbital period. For that streamline, the inviscid growth rate is still strongly positive. Decreasing viscosity, for the global mode calculation only, leads to a reduction in the global mode period, corresponding to the instability being centred closer to the cylinder surface, where the inviscid growth rate is higher. Thus, it does not seem that the generalized inviscid instability theory, even adjusted for the first-order effects of viscosity, can supply quantitative estimates of the growth rate or the preferred wavelength, although it certainly is qualitatively consistent with many features of the inviscid predictions.

5.3.9. *The mode G instability*

   The last three-dimensional mode discovered for this parameter space is mode G. This mode grows on the unsteady base flow, for rotation rates near the upper limit for the existence of the unsteady flow, occurring over a narrow region around $\alpha = 1.85$ for
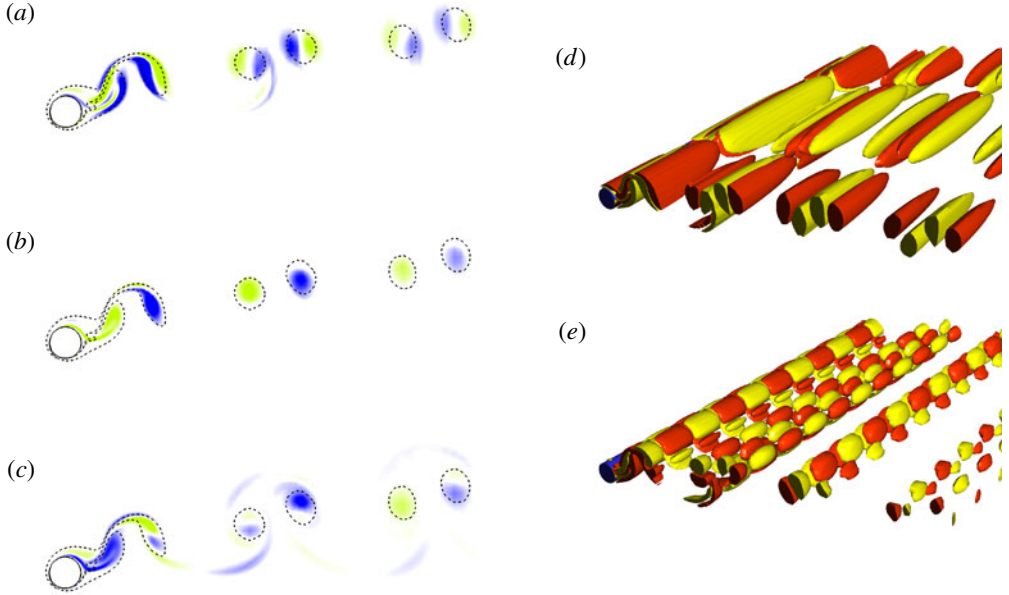
FIGURE 22. (Colour online) Perturbation vorticity contours in the wake of the rotating cylinder at $\alpha = 1.85$ and $Re = 330$ at $\lambda/D = 20$, at an arbitrary time in the shedding cycle: (*a*) spanwise vorticity, (*b*) streamwise vorticity. The streamwise contours of the mode A instability occurring at $\lambda/D = 3.75$ at the same rotation rate and Reynolds number are shown in (*c*). The perturbation contour levels are between $0.1U/D$ with the base-flow vorticity contours at levels $\pm 1U/D$ overlaid as dashed lines. The three-dimensional reconstruction of the mode G and mode A instabilities at $\alpha = 1.85$ and $Re = 330$ are shown in (*d*) and (*e*), respectively. Flow is from left to right in all images.

$Re \geqslant 280$. This is a long-wavelength mode, with a characteristic wavelength $\lambda/D \simeq 18$. This mode has a purely real Floquet multiplier.

Shown in figure 22(*a,b*) are the spanwise and streamwise perturbation vorticity contours, respectively, at $\alpha = 1.85$ and $Re = 330$. The spatial structure of this instability is similar to that of the mode A instability, except for a small apparent phase shift of the perturbation relative to the base flow in the downstream vortices. The streamwise vorticity of the mode A instability at $\lambda/D = 3.75$ at the same rotation rate and Reynolds number is shown in figure 22(*c*) for comparison. Figures 22(*d*) and 22(*e*) show the three-dimensional reconstruction of the spanwise perturbation vorticity fields for mode G and mode A instabilities, respectively.

6. Discussion of the modes spanning the parameter space

A summary of the modes is shown in table 2. For the cylinder spinning at low rotation rates, the onset of the three-dimensional modes is similar to that observed for the non-rotating cylinder; that is, mode A occurs first with increasing Re, prior to the onset of mode B instability. This is essentially due to the similarities in base flow; the structure of the Bérnard–von Kármán vortex street is only changed slightly by the body rotation at these values of α. However, for $\alpha \gtrsim 1.3$, the wake structure becomes strongly asymmetric. Consistent with previous studies where the loss of wake symmetry leads to a different three-dimensional mode being observed, a subharmonic
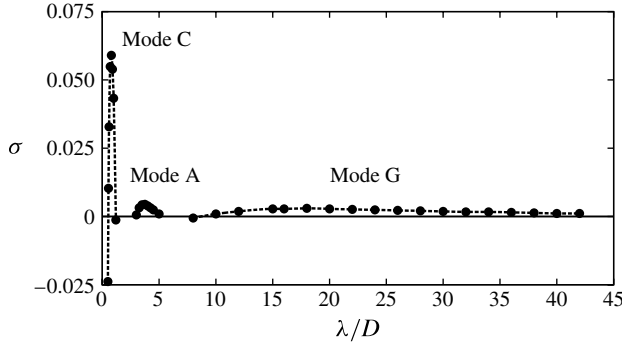
FIGURE 23. Growth rate curves showing the three modes which are unstable to perturbations at $\alpha = 1.85$, $Re = 330$.

Mode	λ/D	Nature of μ	Base flow	Symmetry
A	$\simeq 4$	Real and positive	Unsteady	$u(x, y, z, t) = u(x, y, z + n\lambda, t + T)$
B	$\simeq 0.8$	Real and positive	Unsteady	$u(x, y, z, t) = u(x, y, z + n\lambda, t + T)$
C	$\simeq 1$	Real and negative	Unsteady	$u(x, y, z, t) = u(x, y, z + n\lambda, t + 2T)$
D	$\simeq 1.9$	Real and positive	Unsteady	$u(x, y, z, t) = u(x, y, z + n\lambda, t + T)$
E	$\simeq 1.8$	Real and positive	Steady	$u(x, y, z, t) = u(x, y, z + n\lambda)$
F	$\simeq 0.4$	Complex	Steady	$u(x, y, z, t) = u(x, y, z + n\lambda, t + T_{3D})$
G	$\simeq 18$	Real and positive	Unsteady	$u(x, y, z, t) = u(x, y, z + n\lambda, t + T)$

TABLE 2. Summary of the modes showing the characteristic wavelength, nature of the Floquet multiplier (μ), the periodicity of the two-dimensional base flow and the spatial symmetries of these modes with respect to the streamwise velocity, u.

mode (mode C) is the first three-dimensional mode to become unstable to spanwise perturbations at these higher α. A mode with these symmetries and characteristics has been observed in earlier studies on flow past rings (Sheard *et al.* 2005*a*). At $\alpha = 1.5$, this mode is unstable for a small range of Reynolds numbers before decaying at higher Reynolds numbers, following which the onset of mode A instability is observed. However, at $\alpha > 1.75$, mode C is found to persist over a larger range of Reynolds numbers; for certain values of Re, multiple three-dimensional modes are predicted to be unstable. An instance of this is shown in figure 23, where modes C, A and G are observed at $\alpha = 1.85$, $Re = 330$. The mode C instability is the fastest growing mode followed by mode G and mode A.

The mode D instability occurs in the high-frequency shedding region at rotation rates in excess of 1.9. Figure 9 shows that mode D exists in a region of the parameter space very close to the steady–unsteady transition of the two-dimensional base flow; in some senses, mode D can be viewed as the 'periodic' state of mode E. Figures 14 and 15 clearly show the similarities in the structure of these two modes.

For a given rotation rate, the spanwise wavelength at which the maximum growth rate of the mode D and E instabilities occurs decreases as Reynolds number is increased. For instance, the mode E instability at $\alpha = 2$, $Re = 220$ (a case just past the onset of three-dimensionality) has a peak wavelength of 1.96D, while at $Re = 340$ the
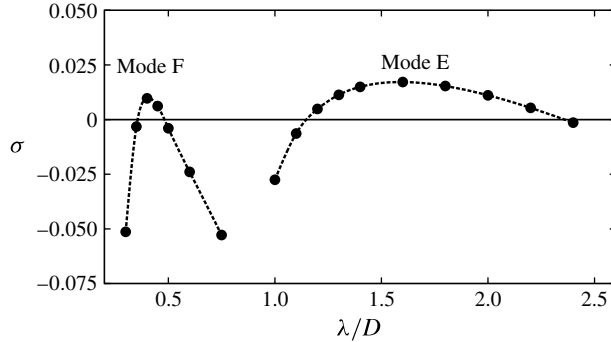
FIGURE 24. Growth rate curves showing the mode E and mode F instabilities at $\alpha = 2.25$, $Re = 320$.

peak wavelength decreases to $1.8D$. Further, as rotation rate is increased from $\alpha = 2$ to $\alpha = 2.25$, the peak wavelength at $Re = 300$ decreases from $1.9D$ to $1.65D$.

At $\alpha = 2.25$, the mode E instability exists alongside the mode F instability (see figure 24). The short-wavelength instability of mode F has a complex Floquet multiplier, indicating it is periodic as it occurs in the steady regime of flow. The spanwise wavelength is much smaller than that predicted by the DNS of Meena *et al.* (2011) at slightly higher rotation rates. Further analysis of the nature of the instability using the inviscid instability theory of Bayly (1988) is consistent with it being primarily centrifugal in nature, although the influence of viscosity appears too strong for the theory to provide realistic estimates for wavelengths or growth rates.

7. Conclusions

The results of a linear stability analysis for a spinning cylinder in a free stream have been presented. These results build upon the existing knowledge of the three-dimensional wake modes that were first observed in the wake of a non-rotating cylinder by Williamson (1988). The non-dimensionalized rotation rate, α, and Reynolds number, Re, were varied over a wide parameter space to first obtain the base flow over which stability analysis was performed to determine the growth (or decay) of perturbations. Furthermore, stability analysis was used to predict the characteristic wavelength of each instability, and the spatio-temporal symmetries.

At low rotation rates, the change in the structure of the Kármán shedding is minimal, and the onset of the three-dimensional modes resembles that of the non-rotating cylinder, although the critical values for the onset of the mode A and mode B instabilities are delayed to higher Reynolds numbers. At higher rotation rates, a subharmonic mode, mode C, is unstable to the perturbations and is unstable in a closed region of the parameter space. This mode is the first three-dimensional mode which becomes unstable with increasing Re, followed by the onset of the mode A type instability. At higher rotation rates of $\alpha = 1.85$, a long-wavelength instability is observed alongside mode C and mode A instabilities.

For high rotation rates ($\alpha > 2$), the rotation stabilizes the vortex shedding, resulting in a steady two-dimensional base flow. This class of steady base flows has been shown to be unstable to at least two modes: mode E, which appears to be due to amplification of perturbations in the high-strain regions of the near wake; and mode F, which

appears to be consistent with a centrifugal instability of the closed region of flow near the cylinder surface for high rotation rates.

Acknowledgements

REFERENCES

AKOURY, R. EL, BRAZA, M., PERRIN, R., HARRAN, G. & HOARAU, Y. 2008 The three-dimensional transition in the flow around a rotating cylinder. *J. Fluid Mech.* **607**, 1–11.

BADR, H. M., COUTANCEAU, M., DENNIS, S. C. R. & MENARD, C. 1990 Unsteady flow past a rotating circular cylinder at Reynolds numbers 10^3 and 10^4. *J. Fluid Mech.* **220**, 459–484.

BADR, H. M., DENNIS, S. C. R. & YOUNG, P. J. S. 1989 Steady and unsteady flow past a rotating circular cylinder at low Reynolds numbers. *Comput. Fluids* **17** (4), 579–609.

BARKLEY, D. & HENDERSON, R. D. 1996 Three-dimensional Floquet stability analysis of the wake of a circular cylinder. *J. Fluid Mech.* **322**, 215–241.

BARKLEY, D., TUCKERMAN, L. S. & GOLUBITSKY, M. 2000 Bifurcation theory for three-dimensional flow in the wake of a circular cylinder. *Phys. Rev.* E **61**, 5247–5252.

BAYLY, B. J. 1988 Three-dimensional centrifugal-type instabilities in inviscid two-dimensional flows. *Phys. Fluids* **31**, 56–64.

BILLANT, P. & GALLAIRE, F. 2005 Generalised Rayleigh criterion for non-axisymmetric centrifugal instabilities. *J. Fluid Mech.* **542**, 365–379.

BLACKBURN, H. M. & LOPEZ, J. M. 2003 On three-dimensional quasiperiodic Floquet instabilities of two-dimensional bluff body wakes. *Phys. Fluids* **15**, L57–L60.

BLACKBURN, H. M., MARQUES, F. & LOPEZ, J. M. 2005 Symmetry breaking of two-dimensional time-periodic wakes. *J. Fluid Mech.* **552**, 395–411.

CHEN, Y.-M., OU, Y.-R. & PEARLSTEIN, A. J. 1993 Development of the wake behind a circular cylinder impulsively started into rotatory and rectilinear motion. *J. Fluid Mech.* **253**, 449–484.

CHEW, Y. T., CHENG, M. & LUO, S. C. 1995 A numerical study of flow past a rotating circular cylinder using a hybrid vortex scheme. *J. Fluid Mech.* **299**, 35–71.

GALLAIRE, F., MARQUILLE, M. & EHRENSTEIN, U. 2007 Three-dimensional transverse instabilities in detached boundary layers. *J. Fluid Mech.* **571**, 221–233.

GÖRTLER, H. 1955 Dreidimensionales zur stabilitätstheorie laminarer grenzschichten. *Z. Angew. Math. Mech.* **35** (9–10), 362–363.

GRIFFITH, M. D., THOMPSON, M. C., LEWEKE, T., HOURIGAN, K. & ANDERSON, W. P. 2007 Wake behaviour and instability of flow through a partially blocked channel. *J. Fluid Mech.* **582**, 319–340.

INGHAM, D. B. 1983 Steady flow past a rotating cylinder. *Comput. Fluids* **11** (4), 351–366.

KANG, S. M., CHOI, H. C. & LEE, S. 1999 Laminar flow past a rotating circular cylinder. *Phys. Fluids* **11** (11), 3312–3321.

KARNIADAKIS, G. E. & SHERWIN, S. J. 2005 *Spectral/hp Methods for Computational Fluid Dynamics*. Oxford University Press.

KARNIADAKIS, G. E. & TRIANTAFYLLOU, G. S. 1992 Three-dimensional dynamics and transition to turbulence in the wake of bluff objects. *J. Fluid Mech.* **238**, 1–30.

KUMAR, S., CANTU, C. & GONZALEZ, B. 2011 Flow past a rotating cylinder at low and high rotation rates. *J. Fluids Engng* **133** (4), 041201.

LAGNADO, R. R., PHAN-THIEN, N. & LEAL, L. G. 1983 The stability of two-dimensional linear flow. In *Proceedings of the Eighth Australasian Fluid Mechanics Conference*, pp. 7A5–7A7. University of Newcastle.

LEBLANC, S. & GODEFERD, F. S. 1999 An illustration of the link between ribs and hyperbolic instability. *Phys. Fluids* **11** (2), 497–499.

LEONTINI, J. S., THOMPSON, M. C. & HOURIGAN, K. 2007 Three-dimensional transition in the wake of a transversely oscillating cylinder. *J. Fluid Mech.* **577**, 79–104.

LEWEKE, T. & WILLIAMSON, C. H. K. 1998 Cooperative elliptic instability of a vortex pair. *J. Fluid Mech.* **360**, 85–119.

MAMUN, C. K. & TUCKERMAN, L. S. 1995 Asymmetry and Hopf-bifurcation in spherical Couette flow. *Phys. Fluids* **7** (1), 80–91.

MEENA, J., SIDHARTH, G. S., KHAN, M. H. & MITTAL, S. 2011 Three-dimensional instabilities in flow past a spinning and translating cylinder. In *IUTAM Symposium on Bluff Body Flows*, IIT-Kanpur, India, pp. 59–62.

MITTAL, S. 2004 Three-dimensional instabilities in flow past a rotating cylinder. *J. Appl. Mech.* **71** (1), 89–95.

MITTAL, S. & KUMAR, B. 2003 Flow past a rotating cylinder. *J. Fluid Mech.* **476**, 303–334.

PRALITS, J. O., BRANDT, L. & GIANNETTI, F. 2010 Instability and sensitivity of the flow around a rotating circular cylinder. *J. Fluid Mech.* **650**, 513–536.

PRANDTL, L. 1926 Application of the 'Magnus effect' to the wind propulsion of ships, National Advisory Committee for Aeronautics, Technical memorandum, 367.

RAO, A., STEWART, B. E., THOMPSON, M. C., LEWEKE, T. & HOURIGAN, K. 2011 Flows past rotating cylinders next to a wall. *J. Fluids Struct.* **27** (5–6), 668–679.

RAYLEIGH, LORD 1917 On the dynamics of revolving fluids. *Proc. R. Soc. Lond.* A **93**, 148–154.

SHEARD, G. J. 2011 Wake stability features behind a square cylinder: focus on small incidence angles. *J. Fluids Struct.* **27** (5–6), 734–742.

SHEARD, G. J., FITZGERALD, M. J. & RYAN, K. 2009 Cylinders with square cross-section: wake instabilities with incidence angle variation. *J. Fluid Mech.* **630**, 43–69.

SHEARD, G. J., THOMPSON, M. C. & HOURIGAN, K. 2003 From spheres to circular cylinders: the stability and flow structures of bluff ring wakes. *J. Fluid Mech.* **492**, 147–180.

SHEARD, G. J., THOMPSON, M. C. & HOURIGAN, K. 2005a Subharmonic mechanism of the mode C instability. *Phys. Fluids* **17** (11), 1–4.

SHEARD, G. J., THOMPSON, M. C., HOURIGAN, K. & LEWEKE, T. 2005b The evolution of a subharmonic mode in a vortex street. *J. Fluid Mech.* **534**, 23–38.

SIPP, D. & JACQUIN, L. 2000 Three-dimensional centrifugal-type instabilities of two-dimensional flows in rotating systems. *Phys. Fluids* **12**, 1740–1748.

STEWART, B. E., HOURIGAN, K., THOMPSON, M. C. & LEWEKE, T. 2006 Flow dynamics and forces associated with a cylinder rolling along a wall. *Phys. Fluids* **18** (11), 111701.

STEWART, B. E., THOMPSON, M. C., LEWEKE, T. & HOURIGAN, K. 2010 The wake behind a cylinder rolling on a wall at varying rotation rates. *J. Fluid Mech.* **648**, 225–256.

STOJKOVIĆ, D., BREUER, M. & DURST, F. 2002 Effect of high rotation rates on the laminar flow around a circular cylinder. *Phys. Fluids* **14** (9), 3160–3178.

STOJKOVIĆ, D., SCHÖN, P., BREUER, M. & DURST, F. 2003 On the new vortex shedding mode past a rotating circular cylinder. *Phys. Fluids* **15** (5), 1257–1260.

THOMPSON, M. C., HOURIGAN, K., CHEUNG, A. & LEWEKE, T. 2006a Hydrodynamics of a particle impact on a wall. *Appl. Math. Model.* **30**, 190–196.

THOMPSON, M. C., HOURIGAN, K., RYAN, K. & SHEARD, G. J. 2006b Wake transition of two-dimensional cylinders and axisymmetric bluff bodies. *J. Fluids Struct.* **22**, 793–806.

THOMPSON, M. C., HOURIGAN, K. & SHERIDAN, J. 1996 Three-dimensional instabilities in the wake of a circular cylinder. *Exp. Therm. Fluid Sci.* **12**, 190–196.

THOMPSON, M. C., LEWEKE, T. & WILLIAMSON, C. H. K. 2001 The physical mechanism of transition in bluff body wakes. *J. Fluids Struct.* **15**, 607–616.

WILLIAMSON, C. H. K. 1988 The existence of two stages in the transition to three-dimensionality of a cylinder wake. *Phys. Fluids* **31**, 3165–3168.

WILLIAMSON, C. H. K. 1996a Three-dimensional vortex dynamics in bluff body wakes. *Exp. Therm. Fluid Sci.* **12**, 150–168.

WILLIAMSON, C. H. K. 1996*b* Three-dimensional wake transition. *J. Fluid Mech.* **328**, 345–407.

WILLIAMSON, C & BROWN, G. L. 1998 A series in $1/\sqrt{Re}$ to represent the Strouhal–Reynolds number relationship of the cylinder wake. *J. Fluids Struct.* **12**, 1073–1085.

ZHANG, H.-Q., FEY, U., NOACK, B. R., KONIG, M. & ECKELEMANN, H. 1995 On the transition of the cylinder wake. *Phys. Fluids* **7** (4), 779–794.